## Title

Sulfur-based thermal energy storage system using intermodal containment: Design and performance analysis



## Authors

Shinn, M
Nithyanandam, K
Barde, A
et al.

## Publication Date

2018

## DOI

10.1016/j.applthermaleng.2017.08.167

Peer reviewed

Applied Thermal Engineering 128 (2018) 1009–1021

Contents lists available at ScienceDirect

Applied Thermal Engineering

journal homepage: www.elsevier.com/locate/apthermeng

Research Paper

# Sulfur-based thermal energy storage system using intermodal containment: Design and performance analysis

M. Shinn, K. Nithyanandam *, A. Barde, R.E. Wirz

*Energy Innovation Laboratory, Department of Mechanical and Aerospace Engineering, University of California, Los Angeles, Los Angeles, CA, 90095, United States*

## HIGHLIGHTS

- Elemental sulfur is a promising low-cost candidate for thermal energy storage.
- Transient performance of sulfur-based shell and tube thermal battery is investigated.
- Results show preferred designs that provide high exergetic efficiency and low system cost.

## ARTICLE INFO

*Article history:*
Received 4 April 2017
Revised 14 July 2017
Accepted 31 August 2017
Available online 1 September 2017

*Keywords:*
Thermal energy storage (TES)
Elemental sulfur
Exergetic efficiency
System model
Intermodal container

## ABSTRACT

Thermal energy storage (TES) is an important energy storage technology that can be coupled to intermittent energy sources to improve system dispatchability. Elemental sulfur is a promising candidate storage fluid for high temperature TES systems due to its high energy density, moderate vapor pressure, high thermal stability, and low cost. This study uses a transient, two-dimensional numerical model to investigate the design and performance of a thermal energy storage (TES) system that uses sulfur stored isochorically in an intermodal shell and tube thermal battery configuration. Parametric analyses of key design and operating parameters show that there is a preferred tube diameter based on the competing influence of system-level energy storage utilization, exergetic efficiency, and cost. The results show that designs with smaller tube dimensions in the range of 2″ NPS to 4″ NPS provide exergetic efficiencies close to 95% while tube dimensions in the range of 4″ NPS to 8″ NPS meet the Department of Energy cost target of $15/kWh with costs being as low as $8.41/kWh. Finally, a table of preferred designs that meet the DOE cost goals is presented to help guide future design and experimentation efforts.



## 1. Introduction

Thermal energy storage (TES) can reduce the variability of renewable power generation and increase dispatchability. For example, in the case of concentrating solar power (CSP), during times of intermittency such as at night or during heavy cloud cover, fuel based backup systems are commonly employed to guarantee a constant generation capacity, especially during periods of peak demand [1]. The integration of TES will allow for the removal of greenhouse gas producing fossil fuel based backup systems. Along with making CSP plants more dispatchable, TES typically have lower capital costs than mechanical and chemical methods of storage, and it has been shown to increase the annual capacity factor of CSP plants [2]. Outside of its use in CSP, strategies for improving the performance of combined heat and power (CHP) plants with TES [3] have been investigated in an effort to improve the overall system efficiency and cost. In addition, future opportunities for use in waste heat recovery systems in industrial processes such as pulp and paper mills, glassmaking, and metallurgy exist due to the high quality waste heat produced [4,5]. Due to its use in a number of different industries and important role in renewable energy, there is an interest in developing accurate simulation tools for the design of TES systems.

The state of the art TES involves sensible storage in a two-tank system using molten salt as a thermal storage material (typically eutectic mixture of 60% sodium nitrate and 40% potassium nitrate) [6]. While two tank systems can be used in both parabolic trough and central receiver CSP configurations up to temperatures of 565 °C without thermal degradation of the storage fluid, the relatively high storage cost of $80/kWh$_t$ of building these systems does not satisfy the technoeconomic target cost of less than $15/kWh$_t$ put forth by the US Department of Energy (DOE) and thus presents an economic dilemma [7,8]. Reductions in storage cost can be

* Corresponding author.
*E-mail address:* kartn87@ucla.edu (K. Nithyanandam).

https://doi.org/10.1016/j.applthermaleng.2017.08.167
1359-4311/

**Nomenclature**

| | |
|---|---|
| $A_c$ | cross sectional area [$m^2$] |
| $b_c$ | baffle cut [%] |
| $b_s$ | baffle spacing [m] |
| $c_{cont}$ | cost of an intermodal container [$/container] |
| $c_p$ | specific heat [J/kg K] |
| $c_s$ | cost of sulfur [$/kg] |
| $c_t$ | cost of tube material [$/kg] |
| $c_w$ | welding cost [$/m] |
| $C_{TES}$ | total cost of thermal storage system [$/$kWh_t$] |
| $CL$ | tube layout constant |
| $CTP$ | tube count constant |
| $d$ | diameter [m] |
| $E_{th}$ | stored energy [J] |
| $f$ | friction factor |
| $h$ | heat transfer coefficient [W/$m^2$ K] |
| $H$ | height of container [m] |
| $j$ | Colburn j-factor |
| $J$ | Bell-Delaware heat transfer correction coefficient |
| $k$ | thermal conductivity [W/m K] |
| $L$ | system length [m] |
| $L_w$ | weld length for a system, $L_w = 2\pi d_o N_t$ [m] |
| $m$ | mass of material [kg] |
| $\dot{m}$ | mass flow rate [kg/s] |
| $n$ | specific heat ratio |
| $N_b$ | number of baffles |
| $N_c$ | effective number of tube rows crossed between baffle tips |
| $N_{cw}$ | effective number of tube rows crossed in the flow window |
| $N_t$ | number of tubes |
| $P$ | perimeter [m] |
| $P_t$ | tube pitch [m] |
| $P_r$ | tube pitch ratio, $P_r = P_t/d_o$ |
| $Pr$ | Prandtl number |
| $Q_{cap}$ | storage capacity [J] |
| $R$ | specific ideal gas constant [J/kg K] |
| $R_1$ | Bell-Delaware method pressure correction coefficient |
| $S_m$ | tube bundle crossflow area [$m^2$] |
| $S_w$ | baffle window flow area [$m^2$] |
| $t$ | time [s] |
| $T$ | temperature [°C] |
| $U$ | energy utilization [%] |
| $W$ | width of container [m] |
| $W_f$ | turbomachinery energy [J] |
| $z$ | axial location [m] |

*Greek symbols*

| | |
|---|---|
| $\alpha$ | thermal diffusivity ($\alpha = k/\rho c_p$) [$m^2$/s] |
| $\Delta P$ | nozzle to nozzle shell-side pressure drop [Pa] |
| $\varepsilon$ | exergy [J] |
| $\rho$ | density [kg/$m^3$] |
| $\mu$ | dynamic viscosity [kg/m s] |
| $\theta$ | tube layout (angle) |
| $\phi$ | wall viscosity compensation term |
| $\eta$ | turbomachinery efficiency [%] |
| $\psi$ | exergetic efficiency [%] |

*Subscripts and superscripts*

| | |
|---|---|
| $C$ | charge |
| $D$ | discharge |
| f | shell side heat transfer fluid |
| i | inner |
| o | outer |
| s | sulfur |
| w | tube wall |
| 0 | dead state value |

*Acronyms*

| | |
|---|---|
| CSP | Concentrated Solar Power |
| CFD | Computational Fluid Dynamics |
| DOE | Department of Energy |
| HTF | Heat Transfer Fluid |
| NPS | Nominal Pipe Size |
| PCM | Phase Change Material |
| STTB | Shell and Tube Thermal Battery |
| TEMA | Tubular Exchanger Manufacturers Association, Inc. |
| TES | Thermal Energy Storage |

achieved by developing high density and low cost TES using inexpensive storage materials.

One proposed storage material for implementation in TES systems which meets the DOE goals of high heat transfer performance, low cost (<15 $/kWh$_t$), and high thermal and chemical stability to above 1000 °C is elemental sulfur [9]. Elemental sulfur has high gravimetric and volumetric energy storage density due to contributions from sensible, latent, and thermochemical enthalpies. Sulfur has a moderate vapor pressure that reduces the amount of material necessary for containment and exhibits low pressures below 200 psig at 600 °C [10]. Due to the elemental stature of sulfur, it exhibits excellent chemical stability at higher operating temperatures [11]. Unlike molten salts, sulfur does not exhibit thermal degradation at high temperatures and can operate at higher temperatures for a superior Carnot efficiency. The nominal cost of sulfur, typically $0.06–0.16/kg [12,13], is far less than typical molten salts and low temperature oils which cost between $1.19/kg – $5.00/kg and $0.30/kg – $5.00/kg [14]. Wong et al. [15] have previously demonstrated the use of an elemental sulfur based thermochemical storage cycle with energy stored via decomposition of sulfuric acid and recovered via combustion of elemental sulfur. Additionally, both Clark and Dowling [16] as well as Wentworth and Chen [17] have proposed TES using elemental sulfur and sulfur based compounds, respectively, in an isobaric configuration. An isochoric sensible TES configuration has not been demonstrated, but has been proposed by Wirz et al. [18] and is considered here for study.

Numerous experimental and numerical studies using shell and tube configurations for TES systems have been led. Lacroix [19] developed an experimentally validated numerical model that predicted the transient multiphase behavior of shell-side PCM charged and discharged by a tube-side heat transfer fluid. He and Zhang [20], and Trp [21] both performed experimental tests and theoretical analysis for similar TES configurations with PCM and paraffin waxes, respectively, on the shell-side and found that the numerical and experimental results agreed very well. Ganapathi et al. [22] constructed a 5 kWh$_t$ lab scale demonstration using supercritical naphthalene as the tube-side storage fluid, and Tse et al. [23] have shown that such systems can be optimized for a maximum exergetic efficiency of 87% using synthetic oil based HTF on the shell-side. For conventional shell and tube style TES geometries, we propose the use of intermodal shipping containers in TES systems due to their standard sizing and use in global transport of products, which forms the subject of investigation in the present study.

Previous studies using air as HTF have been conducted using packed bed systems [24–27]. For this study, air is considered as HTF due to its inexpensive material cost in comparison to conventional molten salt HTF, the increased focus on the development of air-Brayton engines for power cycles [28], and the development of volumetric receiver technologies for use in next generation central receiver systems in CSP plants [29]. Because open volumetric receivers exist in an open loop, gaseous HTF can readily be taken from ambient temperatures, heated, and used to fully charge a storage system if desired – a process that is not currently viable for closed loop molten salt based systems due to tubular receiver inlet temperature limitations. While air is the only HTF considered in this study, extensive studies using magnetic nanofluids have also been undertaken for use in high temperature applications such as cooling blankets for fusion reactors and crystal growth, and warrant further investigation [30,31].

The objective of this study is to develop a transient, two-dimensional numerical model to investigate the design and performance of a thermal energy storage (TES) system that uses low cost elemental sulfur stored isochorically in an intermodal shell and tube thermal battery (STTB) configuration. The governing energy equations for the heat transfer fluid, tubes, and storage media are solved via a finite volume method and by implementing empirical correlations for heat transfer and pressure drop within shell and tube system. The model is validated by comparison to experimental results as well as thorough comparison with an analytical solution for the classical Schumann model [32]. The influence of design and operating parameters on the discharge performance of the system is evaluated on the basis of energy utilization, exergetic efficiency, and cost. While experiments and higher order models can provide more accurate and comprehensive results, the short runtime of this numerical model allows for design parameters to be quickly iterated in order to provide results useful for preliminary design and system cost estimation. Finally, the model herein considers elemental sulfur as the TES medium due to it satisfying DOE metrics and having favorable characteristics in comparison to other materials assessed, but other media can be employed using this model for which adequate data for validation exists.

## 2. System description and assumptions

The TES configuration considered in the present study is shown in Fig. 1. For this study, the dimensions of the shell are taken to be that of a standard intermodal shipping container, of which a picture and computer aided design are shown [33]. The shell is defined by a height, $H$, width, $W$, and length, $L$. Within the shell, tubes with an outer diameter, $d_o$, and inner diameter, $d_i$, are packed with the storage medium (sulfur), arranged horizontally, and are supported via baffles that have a central spacing of $b_s$. Tubes are arranged with a triangular layout ($\theta = 30^\circ$) and are separated by a tube pitch, $P_t$. The HTF flows along a tortuous path during charge and discharge with the solid (dotted) arrows indicating the direction of flow during charging (discharging). During the charging (heating) period, hot HTF enters the shell-side at the inlet located at $z = 0$, transfers heat to the cold storage fluid, and then exits at a lower temperature through the outlet at $z = L$. During stand-by period, there is no flow of HTF on the shell-side and heat transfer within the system is dominated by axial conduction which redistributes thermal energy within the system and reduces the axial temperature gradient formed in the system during charging. During discharge, cold HTF enters the system at $z = L$, is heated by the storage fluid, and then exits on the opposite end at $z = 0$ and, having recovered the stored thermal energy, can be used either in a power block for electricity generation or to meet industrial heating requirements.

For this analysis, the shell-side flow of heat transfer fluid is assumed to be incompressible. The outer surface of the system is assumed to be adiabatic, and the HTF temperature is assumed to be radially invariant while varying in the axial direction. The temperature of the tube wall (stainless steel 316) and sulfur inside each tube is assumed uniform in the radial direction while varying in the axial direction at any given instant of time. The assumption of radial uniformity in the tube wall for any given axial location is valid due to its relatively low conductive thermal resistance [34]. While the storage medium does not exhibit radial uniformity, the convective heat transfer correlation given by Nithyanandam et al. [35] provides an accurate measure of the volume averaged

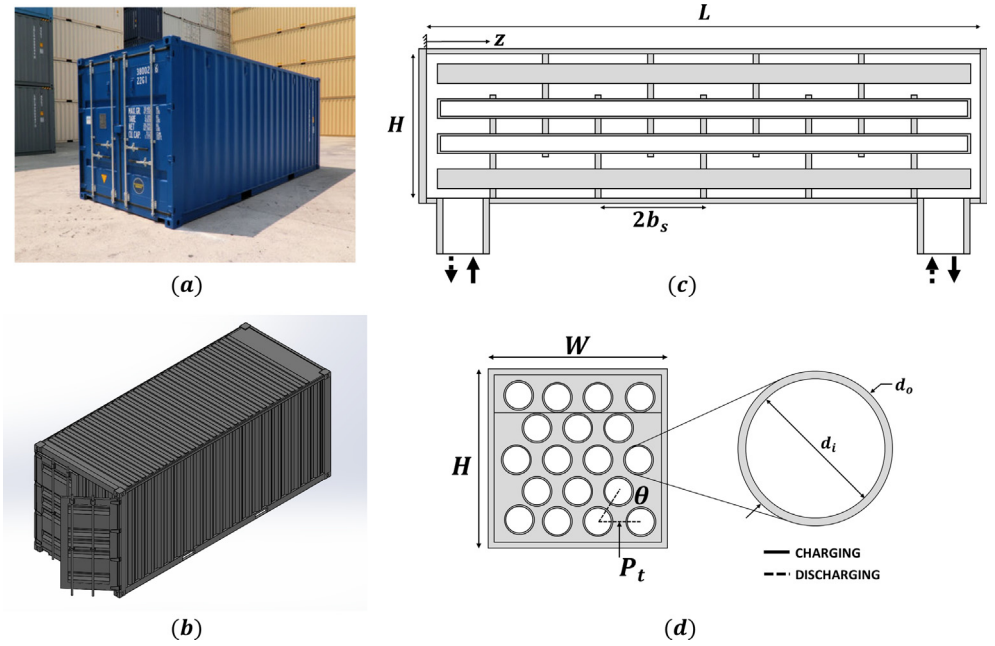


**Fig. 1.** (a) Intermodal container that makes up shell portion of shell and tube thermal battery system [33], (b) computer aided design of intermodal container shell [33], (c) sulfur based TES system within container, and (d) cross sectional view of system.

**Table 1**
Thermo-physical properties of sulfur [36], wall, and HTF [34].

| Properties | Sulfur | Wall (SS 316) | Air |
|---|---|---|---|
| Density, $\rho$ [kg/m$^3$] | 1576.8 | 7798.3 | 0.5409 |
| Specific heat, $c_p$ [J/kg K] | 1226.5 | 558.3 | 1069.3 |
| Viscosity, $\mu$ [kg/m s] | – | – | $3.23e-5$ |
| Thermal conductivity, $k$ [W/m K] | 0.16 | 26.1 | 0.05 |

temperature within the storage medium and is used here. The thermophysical properties of sulfur, steel, and air are taken to be the average value for the temperature range considered using data from [34,36] and are given in Table 1.

## 3. Numerical model

### 3.1. Governing equations

The governing energy equations for the HTF, wall, and storage medium are denoted by Eqs. (1)–(3) as adopted by Tse et al. [8,23]

$$\frac{\partial T_f}{\partial t}+\left(\frac{\dot{m}}{\rho A_c}\right)_f\frac{\partial T_f}{\partial z}=-\frac{h_o P_o}{(\rho c_p A_c)_f}(T_f-T_w)+\alpha_f\frac{\partial^2 T_f}{\partial z^2} \tag{1}$$

$$\frac{\partial T_w}{\partial t}=\frac{h_o P_o}{(\rho c_p A_c)_w}(T_f-T_w)-\frac{h_i P_i}{(\rho c_p A_c)_w}(T_w-T_s)+\alpha_w\frac{\partial^2 T_w}{\partial z^2} \tag{2}$$

$$\frac{\partial T_s}{\partial t}=\frac{h_i P_i}{(\rho c_p A_c)_s}(T_w-T_s)+\alpha_s\frac{\partial^2 T_s}{\partial z^2} \tag{3}$$

where $\dot{m}_f$, $\rho$, $c_p$, $\alpha$, and $T$ refer to the mass flow rate, density, heat capacity, thermal diffusivity, and temperature, respectively, of the HTF, tube wall, or sulfur storage fluid. Geometric terms such as $A_c$ and $P$ refer to the axial cross section and perimeter, respectively, with the subscripts $o$ and $i$ referring to interactions between the HTF and tube, and tube and storage material, respectively. For this study, $d_o$ and the tube wall thickness are chosen based on the nominal pipe size (NPS) according to ASME standards B36.10M and B36.19M [37]. The interstitial heat transfer coefficients between the HTF and tube walls, and the tube walls and storage fluid are represented by $h_o$ and $h_i$, respectively. In Eqs. (1)–(3), $f$ refers to the heat transfer fluid, $w$ refers to the wall, and $s$ refers to the storage material (sulfur). Eqs. (1)–(3) are discretized using a finite volume approach. A hybrid scheme is used to discretize the convective terms, while the diffusion terms are discretized using a central differencing scheme under the assumption of a piecewise-linear profile. Time-stepping of the unsteady term is via a first order fully implicit scheme [38]. A systematic grid and time step study is used to reduce the discretization error, and details of this study are given in the numerical model verification section.

The interstitial heat transfer coefficients are obtained from two different sources. The tube-side heat transfer coefficient is a function of the tube-side Rayleigh number and is obtained via an experimentally validated CFD model, the details of which can be found in the works of Nithyanandam et al. [35]. For systems utilizing shell and tube style heat exchangers – which have analogous shell-side geometry to that of STTB – several studies have employed Kern's method [39], the Bell-Delaware method [40], and Wills-Johnson method [41] in order to quantify the shell-side heat transfer coefficient and pressure drop. For this study, the Bell-Delaware method is utilized because it takes into account the effect of numerous geometric terms affecting fluid flow and heat transfer performance, which are accounted for via the coefficients, $J$ and $R_1$, which are here taken to be 1.054 and 1.0, respectively. The corrected heat transfer coefficient is denoted as:

$$h_o=J\phi c_{p_f} j\frac{\dot{m}_f}{S_m}Pr_f^{-2/3} \tag{4}$$

where $S_m$ is the crossflow area at the shell centerline and is represented by $S_m=b_s\left[\frac{(W-d_o)}{P_t/d_o}(P_t/d_o-1)\right]$, $Pr_f$ is the Prandtl number for the shell-side fluid, $\phi$ is the wall viscosity compensation term ($\phi=\left(\frac{\mu(T=T_w)}{\mu(T=T_f)}\right)^{0.14}$), and $j$ is the Colburn factor which is based on empirical measurements of tube banks in crossflow [42,43]. The nozzle to nozzle pressure drop, $\Delta P$, encompasses the pressure drop due to crossflow, axial flow within the baffle window, and cross flow at the inlet and outlet of the system, and is represented by:

$$\Delta P=R_1\left[(N_b-1)+\left(1+\frac{N_{cw}}{N_c}\right)\right]\left(\frac{2fN_c}{\rho\phi}\left(\frac{\dot{m}_f}{S_m}\right)^2\right)+R_1\left(\frac{(2+0.6N_{cw})\dot{m}_f^2}{2\rho S_m S_w}\right) \tag{5}$$

where $N_c$ and $N_{cw}$ is the effective number of tube rows crossed between baffle tips and in the flow window, respectively, $f$ is the friction factor, and $S_w$ is the net crossflow area through one baffle window given by $S_w=WH-\frac{N_t\pi d_o^2}{4}b_c$. Calculations by Bell et al. [42] determine $N_c$ and $N_{cw}$ as $N_c=H(1-2b_c)/P_t$ and $N_{cw}=0.8b_cH/P_t$. The Bell-Delaware correlation is valid for heat exchangers with square pitch, rotated square pitch, and triangular pitch layouts, and for Reynolds number ($Re_d$) in the range of $1\leqslant Re_d\leqslant 10^5$. The friction factor, $f$, and Colburn factor, $j$, are correlated by Taborek [43] and the coefficients are dependent on the tube layout, tube pitch ratio ($P_r=P_t/d_o$), and Reynolds number. These factors are given as $j=a_1\left(\frac{1.33}{P_r}\right)^a Re_d^{a_2}$ and $f=b_1\left(\frac{1.33}{P_r}\right)^b Re_d^{b_2}$ where the coefficients are tabulated based on empirical results from testing with shell and tube heat exchangers, and further details can be found in the works of Bell [40]. The thermophysical properties of the HTF are shown to greatly affect the shell-side heat transfer coefficient and pressure drop. Thus, for calculation of the shell-side pressure drop and heat transfer coefficient, variable properties of HTF are considered (Table 2). Their temperature dependencies are captured via 4th order polynomial curve fits with data given by Bergman et al. [34].

The pressure drop across the STTB directly affects the turbomachinery energy, $W_f$, required to move the HTF (air) through the system during charging and discharging which in turn affects the overall efficiency of the TES system. Because air can be expressed as a compressible ideal gas, this work can be treated as an isentropic process [44]. This work can be expressed as:

$$W_f=\int_{t_0}^{t_C}\dot{m}_{f,C}\frac{w_C}{\eta}dt+\int_{t_c}^{t_D}\dot{m}_{f,D}\frac{w_D}{\eta}dt \tag{6}$$

where $t_o$ is the initial time and the overall turbomachinery efficiency, $\eta$, is the product of the isentropic compressor efficiency, $\eta_c$, and the energy conversion efficiency, $\eta_{ec}$, (i.e. $\eta=\eta_c\times\eta_{ec}=0.28$). The specific work terms, $w_C$ ($w_D$), during the charge (discharge) cycle are denoted as:

$$w_C=-\frac{nRT(z=L)}{n-1}\left[\left(\frac{P(z=L)}{P(z=L)+\Delta P}\right)^{\frac{n-1}{n}}-1\right] \tag{7}$$

$$w_D=-\frac{nRT(z=0)}{n-1}\left[\left(\frac{P(z=0)}{P(z=0)+\Delta P}\right)^{\frac{n-1}{n}}-1\right] \tag{8}$$

where $n$ is the HTF heat capacity ratio ($n=c_p/c_v=1.4$) and $R$ is the specific ideal gas constant of air ($R=287.058$).

**Table 2**
Variable properties for shell-side HTF coefficient and pressure drop calculations [34].

| Properties | Air HTF |
|---|---|
| Density, $\rho$ [kg/m$^3$] | $(1.52e-12)T^4-(7.35e-9)T^3+(1.29e-5)T^2-9.91T+3.243$ |
| Specific heat, $c_p$ [J/kg K] | $(1.12e-13)T^4-(5.35e-10)T^3+(8.27e-7)T^2-(2.95e-4)T+1.0321$ |
| Viscosity, $\mu$ [kg/m s] | $(-3.97e-13)T^4+(2.15-9)T^3-(4.70e-6)T^2+(6.99e-3)T+0.109$ |
| Thermal conductivity, $k$ [W/m K] | $(3.23e-13)T^4+(1.96e-9)T^3-(5.16e-6)T^2+(1.03e-2)T-0.0640$ |

### 3.2. Boundary conditions

The boundary conditions of the model during charging and discharging are specified as:

$$T_f(z=0)=T_C,\frac{\partial T_f}{\partial z}(z=L)=0;\ \textit{Charging} \tag{9}$$

$$\frac{\partial T_f}{\partial z}(z=0)=0,\frac{\partial T_f}{\partial z}(z=L)=0;\ \textit{Standby} \tag{10}$$

$$T_f(z=L)=T_D,\frac{\partial T_f}{\partial z}(z=0)=0;\ \textit{Discharging} \tag{11}$$

For the first charge (discharge) process the tank is assumed to start from a completely discharged (charged) state. For this study the charge temperature, $T_C$, is taken to be 600 °C and the discharge temperature is taken to be 200 °C, which is well within the temperature range that open volumetric receivers operate in and the tube material can withstand [29].

## 4. Numerical model verification

The numerical model is verified using several techniques. First, time step and grid size dependency studies are conducted in order to reduce the discretization error of the model. Following this study, the heat transfer parameters of the model are verified by two methods. The first method involves comparing the model with experimental results from a single tube sulfur storage system. The results of the experiment are used to properly verify the tube side heat transfer. The second method involves comparison with the analytical solution of a dual-media storage system based on a single phase conductivity model.

### 4.1. Grid size dependency and time step study

Prior to verification, a grid size dependency study and time step study were completed to reduce the discretization error. For this study, the number of axial nodes was increased until the maximum relative error between studies was comparatively small, and further grid refinement led to increased computational cost without providing much more accurate results. The time step study was undertaken in the same manner, in which the dimensionless time step, $\Delta t^* = \frac{\Delta t}{\Delta z}\frac{\dot{m}_f}{\rho S_m}$, was decreased until further refinement did not yield relatively more accurate results. A non-dimensionalized value for time step is used here to account for the effect that the shell-side geometry and HTF has on the crossflow velocity and residence time of the fluid which would not be captured via calculation of $\Delta t$ alone. Fig. 2a and b show the results of said studies for a system with $d_o = 0.06$ m, $b_S = 0.5$ m, $P_r = 1.5$, $\dot{m}_f = 0.5$ kg/s, with all other geometric properties given by Table 3. The result of grid size dependency study is a system with 1000 axial nodes and a maximum relative error of 0.004% were the system to be increased to 3000 axial nodes. The result of the time step study is a non-dimensionalized time step ($\Delta t^*$), of $4.049 \times 10^4$ for a maximum relative error of 0.59%, were the timestep to be decreased to $2.024 \times 10^4$.

### 4.2. Comparison with experimental results

The numerical model presented is verified using results from Refs. [9,45]. A schematic image of the experimental setup is showed in the inset of Fig. 3a. A one meter long, two inch nominal

**Table 3**
Design and operating parameters for single discharge study.

| Parameter | Symbol | Range/Value |
|---|---|---|
| Tube Pitch Ratio | $P_r$ | 1.2 – 1.5 |
| Baffle Spacing | $b_s$ | 2″(0.05 m) – 20″(0.51m) |
| Tube Outer Diameter | $d_o$ | 0.06 m (2″ NPS) – 0.22 m (8″ NPS) |
| Mass Flow Rate | $\dot{m}_f$ | 0.4 kg/s – 3 kg/s |
| Baffle Cut | $b_c$ | 15% |
| Tube Layout Angle | $\theta$ | 30° |
| System Width | $W$ | 2.39 m |
| System Height | $H$ | 2.35 m |
| System Length | $L$ | 5.87 m |

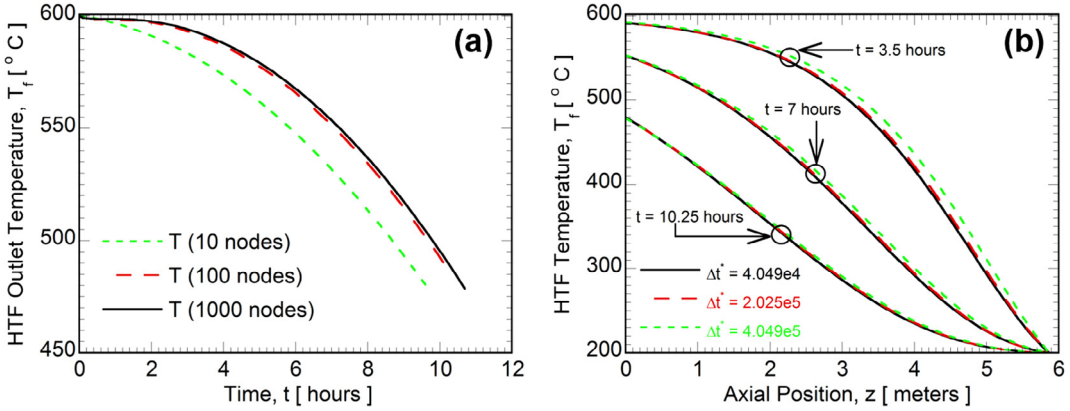


**Fig. 2.** Dependency of numerical solution on (a) grid size, $\Delta z$, and (b) non-dimensional timestep, $\Delta t^*$.

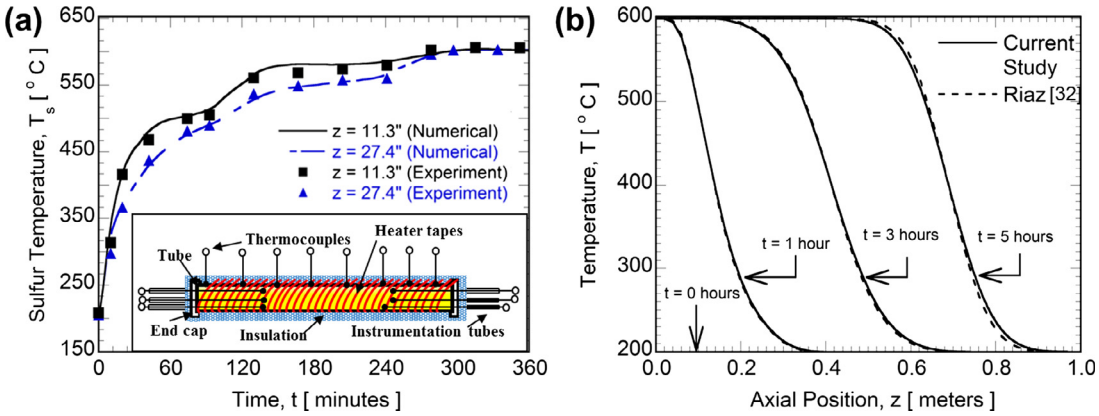


**Fig. 3.** Comparison of numerical results with (a) experimental results [46] and (b) analytical results for a single phase conductivity model by Riaz [32].

pipe size ($d_o = 0.06$ m) schedule 40, stainless steel 316 tube was filled with 3.14 kg of sulfur. Instrumentation tubes are used to provide access to 6 K-type thermocouples with three inserted 11.3″ from the left side of the system and three inserted from the right side of the system with two of those inserted 11.3″ inside and one inserted 8″ inside. The system is heated at the tube wall using eight 300 W heater tapes controlled using PID controllers and covered with ceramic fiber insulation in order to minimize thermal losses to the environment. The surface temperature of the tube was measured using sixteen k-type thermocouples evenly spaced out two inches apart from one another along the entire length of the tube. Due to the experimental setup not involving a HTF, in order to account for heat transfer between the HTF and wall in the numerical mode, $h_o$ was set to an arbitrarily high heat transfer coefficient of $10^{14}$, and $\dot{m}_f$ was set to zero. By doing this, the surface temperature recorded by the experiment could be used as the wall boundary condition inside the model, and the experimental measurements of sulfur temperature could be compared to the sulfur temperature output by the numerical model. Validation using the progressing thermal front condition from Refs. [9,46] is shown in Fig. 3a, with the markers indicating the experimental results and the lines corresponding to results obtained via the model. The model shows good agreement, with the maximum relative error between the numerical results and the experimental results in Fig. 3a being 2.3% and the average error obtained from the Euclidean norm being 2.14%.

### 4.3. Comparison with an analytical model

For further verification, the numerical model was compared with the analytical solution of a simplified Schumann model governing flow of air in a dual-medium storage unit as given by Ref. [32]. In order to compare the numerical model to the analytical solution, a number of simplifications must be made. For this solution, the material properties of the wall were taken to be that of the storage fluid, and $h_o$ was set to an arbitrarily high heat transfer coefficient of $10^{14}$ W/m$^2$ K. Further adjustments of the numerical model such as neglecting the HTF conduction term and a Danckwert type inlet boundary condition, namely $\frac{\partial T_f}{\partial z}(z=0) = \frac{\dot{m}_f c_{p_f}}{A_{c_f} k_s}(T_f - T_C)$, was used in the numerical model to allow for comparison with the analytical solution. For comparison, a test case involving a 1-meter-long system, with $W = 2.352$ m, $H = 2.385$ m, $P_r = 1.2$, and $d_o = 0.06$ m was considered. Comparison between the numerical model and the corresponding results using the analytical solution are shown in Fig. 3b, and the relative error between their results is at a maximum 1.01% and the average error obtained from the Euclidean norm is 0.13%. These validation and verification studies provide sufficient confidence on the veracity of the model and is used for detailed parametric analysis.

## 5. Results and discussion

### 5.1. Single charge, standby, discharge cycle

Prior to conducting a parametric study of a single discharge situation, the response of the system to a single six hour charge, twelve hour standby, and six hour discharge operation is investigated using a parametric combination of $P_r = 1.2$, $d_o = 0.06$ m, $\dot{m}_f = 1.7$ kg/s, and $b_s = 0.5$ m in order to demonstrate the flexibility of the model and explain typical trends seen.

Fig. 4a displays the axial temperature variation of the HTF (solid line) and storage material (dashed line) for different times during charging. The STTB is initially in a fully discharged state ($T = 200\,^{\circ}$C) and there is no flow of fluid through the system. At $t = 0$, HTF enters the system at $z = 0$ and energy is transferred between the HTF and solid material (steel tubes and sulfur). As the HTF gives up its energy, the heat transfer downstream becomes less effective resulting in a nonlinear axial temperature profile. Initially this temperature profile is characterized by HTF near the inlet being at the charge temperature ($T_f(z=0) = T_C$), HTF at the outlet being near the discharge temperature ($T_f(z=L) = T_D$), and the temperature field of the intermediary forming as a result of the stratification of the hot and cold fluid, as typically seen in thermocline storage systems [47]. As charging progresses, the pre-existing cold fluid is discharged from the system and the stratification layer moves across the system. At some point during charging, the outlet temperature will begin to increase as the thermal front reaches the outlet. This temperature profile is also seen in the sulfur, however this profile lags behind the air temperature profile due to sensible heat storage in the tube wall material, as well as due to thermal resistance between the HTF and sulfur. The twelve-hour standby period is shown in Fig. 4b. At the end of charging (t = 6 h), the flow of HTF is halted and the system dynamics are dictated by conduction. Due to the assumption of a well-insulated system, there are no thermal losses to the environment, and all temperature changes within the system are due to heat transfer between the sulfur, tube material, and HTF. Fig. 4b also displays the axial temperature variation of the HTF and storage material for various times during discharge. At $t = 18$ h, HTF enters the system at $z = L$, energy stored inside the storage material (tube wall and sulfur) is recovered by the HTF, and the heated HTF exits the system at $z = 0$. Just as in charging, there is a nonlinear temperature profile that forms in the HTF and the storage material due to the HTF progressively

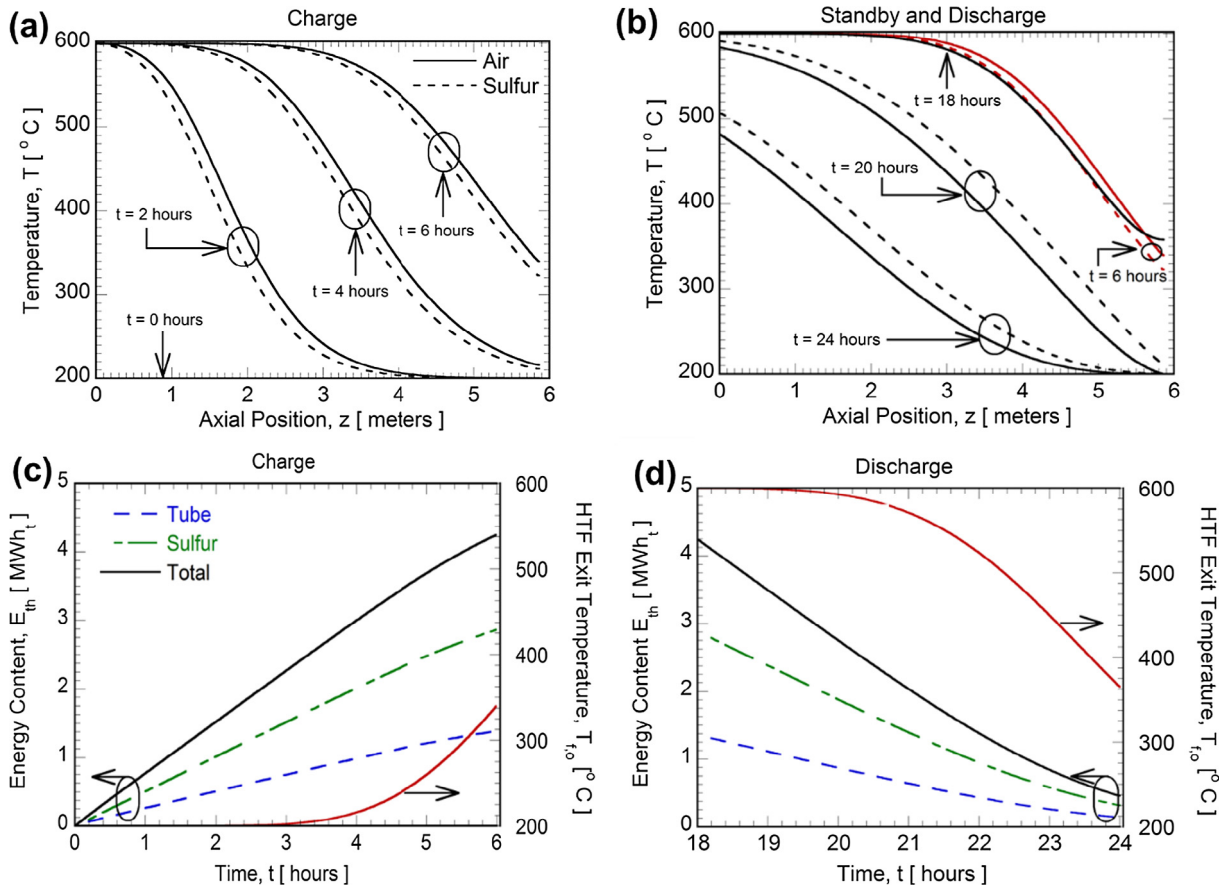


**Fig. 4.** Axial temperature variation of HTF and sulfur during (a) charging and (b) standby (shown in red) and discharging. Energy content as well as HTF outlet temperature during (c) charging and (d) discharge. (For interpretation of the references to colour in this figure legend, the reader is referred to the web version of this article.)

recovering energy from the system, and a delay in the storage material is observable due to the initial recovery of sensible energy in the tube wall material. Ultimately, this discharge process continues until $t = 24$ h at which point the simulation is stopped.

Energy storage within the tube and storage material and the temporal variation in the HTF outlet temperature is shown in Fig. 4c and d. During charging (Fig. 4c) there is a near linear increase in the overall energy stored in the system over time despite there being a nonlinear temperature profile within the system. This is due to the ability of the TES system to absorb all the thermal energy in the HTF until the HTF outlet temperature ($T_f(z = L)$) begins to increase at approximately 4 h. The standby period is characterized by the energy stored within the system being constant due to the assumption of an adiabatic wall condition, and in the interest of conciseness, the standby period energy vs time plot is not shown here. The discharge period is displayed in Fig. 4d. The declining heat transfer temperature ($T_f(z = 0)$) after $t = 21$ h hour leads to a non-linear decay in energy content. Under ideal conditions, all of the thermal energy inside the system should be recovered during the discharge process, however, due to the thermal resistance within the HTF, tube wall, and storage material there is still some thermal energy within the system at the end of discharge.

### 5.2. Parametric study for single discharge

A thermal storage system is designed with the goal of finding the most optimum setup for extending the utilization of a power plant, which in this case is a solar power tower equipped with an open volumetric receiver coupled to a Rankine steam power cycle. The storage system itself is agnostic to the heat input and demand, and a solar power tower and Rankine steam power cycle are considered in order to minimize the number of design and operating parameters for study. The range of design and operating parameters chosen for the TES system are based on typical design ranges seen in shell and tube heat exchangers [42] as well as from typical design constraints chosen for TES in CSP plants [7]. Due to the desire to use standard sizes in order to reduce manufacturing costs and easily transport TES systems; the shell height, width, and length are chosen here to correspond to the dimensions of a 20′ standard intermodal container [33].

A parametric study for a single discharge situation is discussed here in which the system, at a fully charged state ($T = 600$ °C), is discharged by flowing air through the system with air inlet temperature equal to the discharge temperature ($T_D = 200$ °C). Two concurrent cutoff criteria are considered for this study. The first cutoff criterion is based on the HTF outlet temperature with cutoff temperature, $T_{cutoff} = 480$ °C. The temperature cutoff value is based on the requirement that the moisture content of steam at the exhaust of a steam turbine must not exceed 10%, and an analysis using a simple ideal Rankine steam cycle demonstrates that 480 °C is an agreeable cutoff temperature for a system of this storage capacity [26]. The second cutoff criterion is based on the exergetic efficiency of thermal discharging. When the exergy destruction rate due to heat transfer and turbomachinery work exceeds that of the exergy recovery rate from the system during discharge, thermal discharging is stopped. The discharge exergetic efficiency, $\psi_D$, is defined as the total amount of exergy recovered, $\varepsilon_r$, from the system minus exergy destroyed, $\varepsilon_d$, normalized by

the maximum amount of exergy that could be recovered from the system under ideal conditions (i.e. no viscous losses due to pump work and an infinite overall heat transfer coefficient). This can be defined as:

$$\psi_D = \frac{\int_{t_o}^{t_D} \dot{m}_{f,D} c_{p_f} \left( T_{f,out} - T_D - T_0 \ln\left(\frac{T_{f,out}}{T_D}\right)\right) dt - \int_{t_o}^{t_D} \dot{m}_{f,D} \frac{w_p}{\eta} dt}{\int_{t_o}^{t_D} \dot{m}_{f,D} c_{p_f} \left( T_C - T_D - T_0 \ln\left(\frac{T_C}{T_D}\right)\right) dt} \quad (12)$$

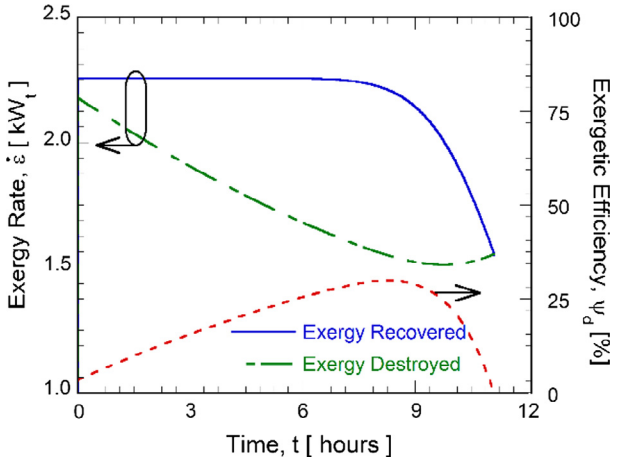


**Fig. 5.** Exergy destruction and recovery, and exergetic efficiency vs time during discharge. Discharge is discontinued at the point at which exergy destruction is equivalent to exergy recovered.

where $T_0$ is the dead state temperature (taken to be 27 °C). The amount of exergy within the system at any given timestep can be represented as:

$$\begin{aligned}\varepsilon(t,T) = \sum_{i=1}^{n} \Big( & m_s c_{p_s} \left[ (T_{s(i)} - T_D) - T_0 \ln\left(\frac{T_{s(i)}}{T_D}\right)\right] \\ & + m_w c_{p_w} \left[ (T_{w(i)} - T_D) - T_0 \ln\left(\frac{T_{w(i)}}{T_D}\right)\right] \\ & + m_f c_{p_f} \left[ (T_{f(i)} - T_D) - T_0 \ln\left(\frac{T_{f(i)}}{T_D}\right)\right] \Big) \Delta z \end{aligned} \quad (13)$$

where $m$ is the mass of the material, $i$ represents the axial node, $n$ corresponds to the total number of discretized axial volumes, and the amount of exergy stored for any given time step is referenced with respect to the discharge temperature, $T_D$, of the system.

To demonstrate the second cutoff criterion, the temporal variation in exergy recovered, exergy destroyed, and exergetic efficiency during discharge for the case of $\dot{m}_f = 1.00$ kg/s, $d_o = 0.06$ m, $P_r = 1.2$, and $b_s = 0.14$ m is shown in Fig. 5. Initially, due to the use of variable properties in calculating the pressure drop of the shell-side HTF, the rate of exergy destroyed, $\varepsilon_d$, will decay with temperature during discharge. As the thermocline layer begins to reach the outlet of the system, the exergy recovered, $\varepsilon_r$, will also begin to decay. For the case considered, the exergy destroyed begins to exceed the exergy recovered before the temperature cut-off criterion is met and it is not sensible to continue heat recovery past this point.

Fig. 6 displays the axial temperature profiles of the storage fluid at the end of discharge for the range of parameters shown in Table 3 and with default parameters given as $P_r = 1.2$, $d_o = 0.06$ m, $\dot{m}_f = 1.75$ kg/s, and $b_S = 0.50$ m. For all plots shown,

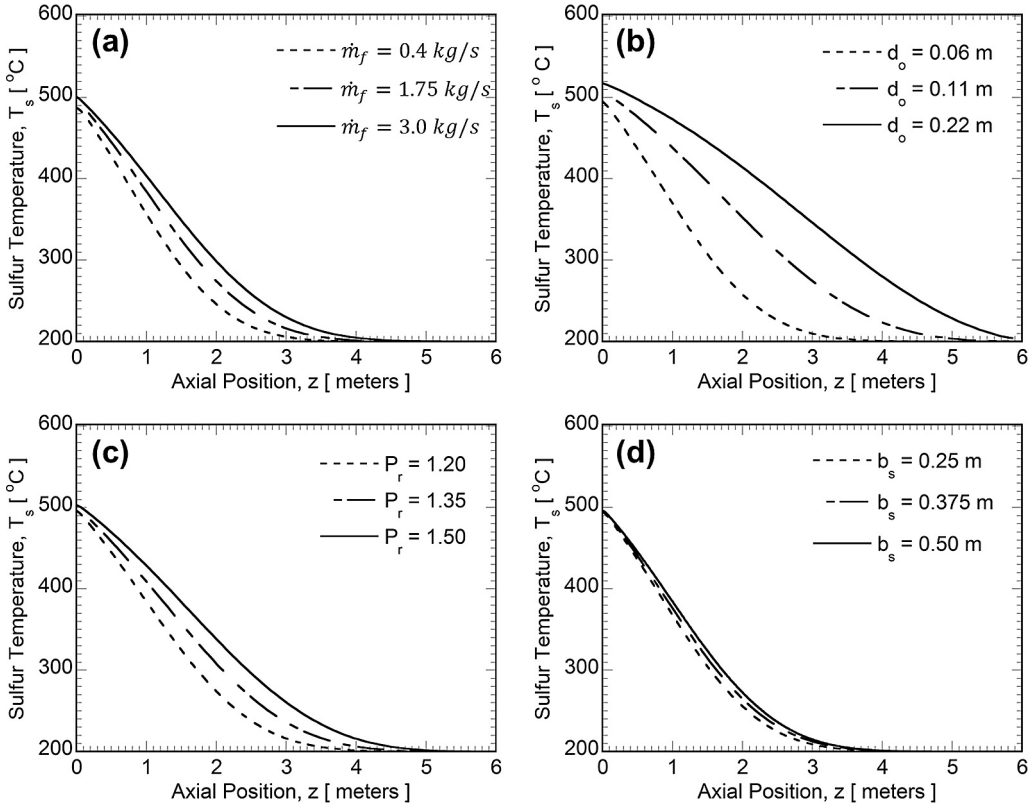


**Fig. 6.** Axial temperature gradient within storage material at the end of discharge for variable (a) mass flow rate, (b) tube outer diameter, (c) tube pitch ratio, and (d) baffle spacing.

the variation in the final axial temperature profile indicates a difference in the amount of energy stored within the system ($E_{th}$) which, at any time step, is represented as:

$$E_{th}(t,T) = \sum_{i=1}^{n}(m_s c_{p_s}(T_{s(i)} - T_D) + m_w c_{p_w}(T_{w(i)} - T_D) + m_f c_{p_f}(T_{f(i)} - T_D))\Delta z \quad (14)$$

Discharge from a fully charged state is evaluated in order to determine the maximum possible utilization, $U$, as defined by Rosen [48]. Discharge utilization is defined as the ratio of the energy recovered from the system by the total storage capacity for given operating temperatures:

$$U = \frac{\int_{t_o}^{t_D} \dot{m}_{f,D} c_{p_f}(T_{f,in} - T_{f,out})dt}{E_{th}(t = t_o, T = T_C)} \quad (15)$$

from the utilization, the utilized storage capacity, $Q_{cap,u} = U \times Q_{cap}$, of a system can be found, and can be useful in comparing between systems that may vary in capacity.

The variation in the final axial temperature profile in the storage material for variable $\dot{m}_f$ is shown in Fig. 6a. The discharge utilization lies between 85.42% and 77.52% for the range of $\dot{m}_f = 0.40$ kg/s to $\dot{m}_f = 3.0$ kg/s, respectively. The trend of increased $U$ with decreased $\dot{m}_f$ is due to the increased residence time of fluid within the system which allows for increased interaction of the HTF with the storage material for energy recovery during discharge. Furthermore, for a dual-medium storage system, a $\dot{m}_f$ results in a relatively low Reynolds number and steeper thermocline [49] which allows for higher quality heat to be recovered and for the temperature cutoff condition to be delayed. However, an increased $\dot{m}_f$ also results in a heightened $h_o$ (Fig. 7a), resulting in improved heat transfer at the cost of an exponentially increased $\Delta P$ (Fig. 7b). The tradeoff between increased exergy recover vs exergy destruction must be weighted in order to find the most efficient operating condition and design point for the system.

The effect of $d_o$ on the final axial temperature profile is shown in Fig. 6b. The increase in $d_o$ leads to lower volumetric heat transfer coefficient resulting in lower rate of thermal discharge. Additionally, larger $d_o$ result in a decreased number of tubes within the system and a decrease in surface area for convective heat transfer to take place. This increases the overall thermal resistance of the system and results in a lower $U$. Thus, more energy is utilized for systems of $d_o = 0.06$ m ($U = 84.25\%$) vs $d_o = 0.22$ m ($U = 60.05\%$).

The effect of tube pitch ratio, $P_r = P_t/d_o$, on the final axial temperature gradient is shown in Fig. 6c. Increased $P_r$ has two major effects on the system. First, for a fixed shell size, the number of tubes within the system, $N_t$, varies depending on the tube pitch ratio, $P_r$. According to Kakaç and Liu [50], $N_t$ can be determined as $N_t = \frac{WH}{(P_r d_o)^2}\frac{CTP}{CL}$, where the variable $CTP$ corresponds to the number of tube passes within the system while CL corresponds to the tube layout. For this study they are chosen to be 0.93 and 0.87, respectively, in order to correspond to a system with a single tube pass and layout of 30° [42]. Increase in $N_t$ provides for more surface area for convective heat transfer and a decreased overall thermal resistance. In addition, as $P_r$ is decreased, the clearance between tubes also decreases. This increases the crossflow Reynolds number and the overall heat transfer coefficient, and allows for superior convective heat transfer for lower $P_r$ despite the decreased residence time of fluid within the system.

The effect of baffle spacing on the discharge axial temperature profile is shown in Fig. 6d. Baffle spacing, $b_s$, is shown to have little effect on the final temperature gradient and U within the system. However, because $\Delta P$ scales nonlinearly with $b_s$, low $b_s$ can result in a high $\Delta P$ and lead to a high amount of exergy destruction due to compressor work. In order to maximize the exergetic efficiency within the system and conform to structural tube support standards set forth by the Tubular Exchanger Manufacturers Association (TEMA) [51], the baffle spacing was chosen to be fixed at 0.5 m for all $\dot{m}_f$ and $d_o$ considered.

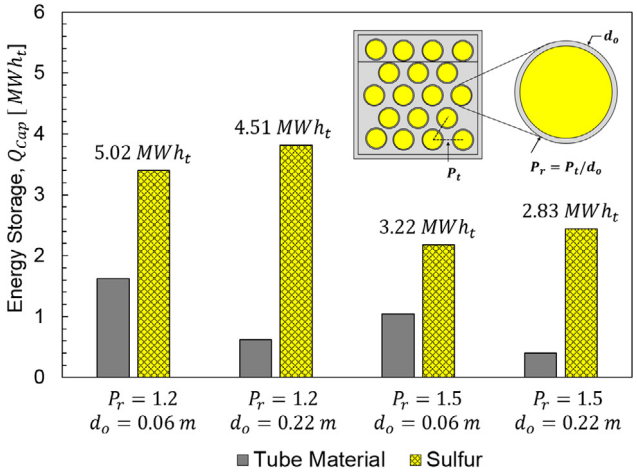


**Fig. 8.** Variation in storage capacity of system based on tube pitch ratio and tube diameter using schedule 10 tubes. Overall storage capacity is shown above each column chart.

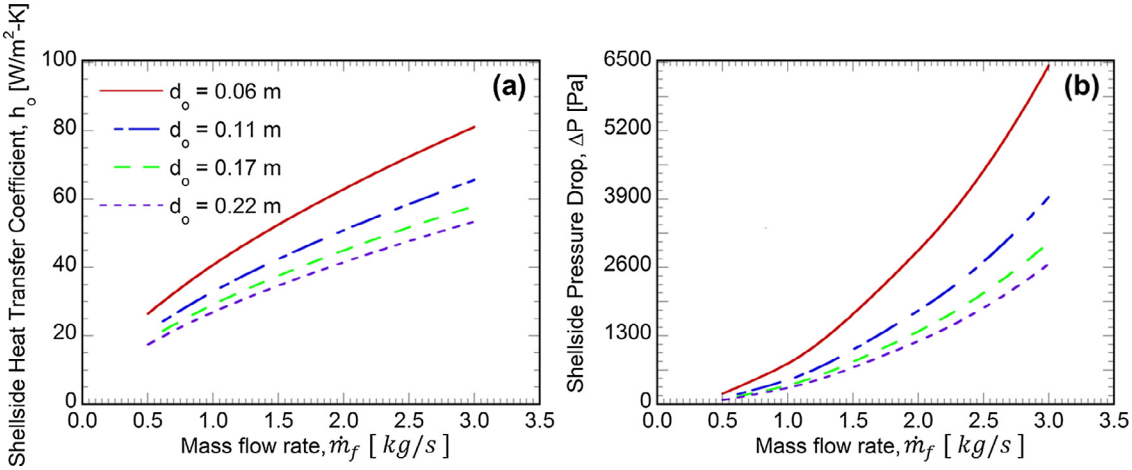


**Fig. 7.** Effect of mass flow rate on (a) shell-side pressure drop and (b) shell-side heat transfer coefficient, for variable tube diameter.

### 5.3. Variable storage capacity study

With $b_s = 0.5$ m, $\psi_D$ and $U$ for a system with a variable storage capacity and air as the shell-side HTF is considered here for study. Because of the fixed shell size, the storage capacity within the system will vary depending on the chosen tube diameter and tube pitch ratio, as seen in Fig. 8. For shell and tube style heat exchangers, TEMA standards dictate that $P_r$ should remain between 1.2 and 1.5, with values falling below this range creating difficulties in cleaning and maintenance, and values above this range leading to poor performance [42]. Fig. 6c shows that the variation in the final axial temperature profile between a system with $P_r = 1.2$ and $P_r = 1.5$ leads to a utilization difference of 6.79%, and thus, in an effort to limit the number of studies, only these two $P_r$ are considered.

Fig. 9a and Fig. 9b show $\psi_D$ vs $\dot{m}_f$ for $P_r = 1.2$ and $P_r = 1.5$. There is a decrease in $\psi_D$ with $\dot{m}_f$ due to the corresponding increased exergy destruction. This increased exergy occurs due to the nonlinear dependence of $\Delta P$ on $\dot{m}_f$ (Eq. (5)), and ultimately leads to the decrease in $\psi_D$ (Eq. (12)). While there is a near linear decrease in $\psi_D$ with $\dot{m}_f$ for $P_r = 1.5$, the nonlinear dependence for $P_r = 1.2$ leads to optimum $d_o$ for different operating conditions, mainly $d_o = 0.11$ m at $\dot{m}_f = 2$ kg/s and $d_o = 0.17$ m at $\dot{m}_f = 3$ kg/s. The difference in $U$ shown in Fig. 9c occurs for multiple reasons. Increased $P_r$ results in fewer tubes within the system, decreased surface area for convective heat transfer, and lower crossflow Reynolds number, all of which are factors reducing the convective heat transfer and decreasing utilization. Due to the difference in tube pitch, nearly all utilized capacities (Fig. 9d) for $P_r = 1.2$ are larger than that of utilized capacities for $P_r = 1.5$ with the exception of the case of $P_r = 1.2$, $d_o = 0.22$ m and $P_r = 1.5$, $d_o = 0.06$ m; for this case both have a similar utilized capacity. The recovery of energy during discharge temporally ($\dot{E}_{out}(t) = \dot{m}_f c_{p_f}(T_{f,out}(t) - T_D)$) and on average

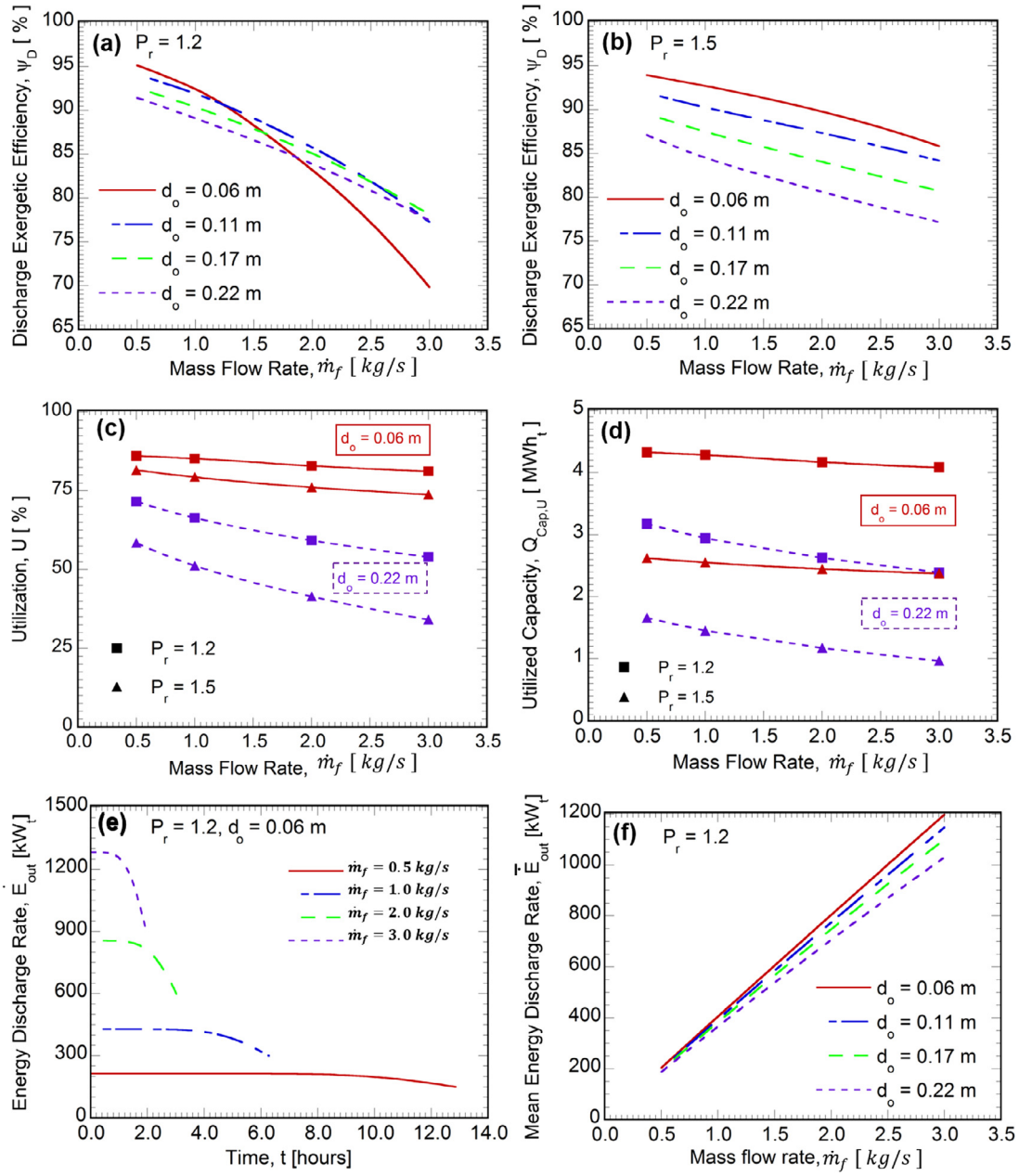


**Fig. 9.** Effect of mass flow rate and tube diameter on the (a) exergetic efficiency for $P_r = 1.2$, (b) exergetic efficiency for $P_r = 1.5$, (c) utilization for $P_r = 1.2$ and $P_r = 1.5$, (d) utilized capacity for $P_r = 1.2$ and $P_r = 1.5$, (e) energy discharge rate vs time for variable mass flow rate, and (f) mean discharge energy rate.

($\bar{\dot{E}}_{out} = \frac{1}{t_d}\int_0^{t_d} \dot{E}_{out}(t)dt$), is shown in Fig. 9e and Fig. 9f, respectively. The operating $\dot{m}_f$ affects the hours of discharge available within a system as seen in Fig. 9e. For a system with $P_r = 1.2$ and $d_o = 0.06$ m, the hours of discharge can vary anywhere between 3 and 13 h, which meet the requirements dictated for both peaker and baseload power plants [28]. Furthermore, for low mass flow rates ($\dot{m}_f = 0.5$ kg/s) the energy recovery during discharge is more consistent with time (i.e. $d\dot{E}_{out}/dt \approx 0$ for low $\dot{m}_f$). Negligible difference in $\bar{\dot{E}}_{out}$ is observed for low mass flow rates ($\dot{m}_f = 0.5$ kg/s), however the difference is more pronounced (168 $kW_t$ for 0.06 m $< d_o <$ 0.22 m) at higher flow rates ($\dot{m}_f = 3.0$ kg/s). This is due to lower utilization of energy for higher tube diameters as seen in Fig. 9c. Fig. 9e and f demonstrate that there is a tradeoff between energy rate that can be delivered and duration of discharge that should be closely considered by a plant operator.

A first order economic analysis shows that the welding cost ($c_w = \$7.50/\text{m} - \$40.00/\text{m}$, [52]) is two to three orders of magnitude higher than that of the price of sulfur ($c_s = \$0.06/\text{kg}$, [13]) and is two to ten times the price of tubes, ($c_t = \$3.00/\text{kg}$, [53]). Thus, welding cost is a driving factor in determining the total cost of a system. The DOE Sunshot Initiative require that the TES system be less than $\$15/\text{kWh}_t$ so that it be cost-competitive with systems that conventionally generate electricity [28]. For comparative purposes, the cost of a TES storage system, $C_{TES}$, can be defined as:

$$C_{TES}\left(\frac{\$}{\text{kWh}_t}\right) = \frac{m_s c_s + m_w c_t + c_{cont} + c_w L_w}{Q_{cap} \times U} \tag{16}$$

where $c_{cont}$ is the cost of an intermodal container ($c_{cont} = \$2000/\text{container}$, [54]), $L_w$ is the weld length for all pipes in a system ($L_w = 2\pi d_o N_t$), and the denominator takes into account the ratio of the nameplate storage capacity utilized. Fig. 10a and b show the influence of $\dot{m}_f$, $c_w$, and $d_o$ on the total system cost. It can be seen that for both $P_r = 1.2$ and $P_r = 1.5$, there exists multiple design points that satisfy the SunShot Initiative target with preferable designs occurring for $d_o > 0.11$ m for most situations. For both $P_r$, the performance saturates past $d_o > 0.17$ m at low flow rates ($\dot{m}_f = 0.5$ kg/s). Additionally, because $U$ is higher for smaller $d_o$, it is desirable to design a system with $d_o \leqslant 0.17$ m to both minimize $C_{TES}$ and maximize $\psi_D$ and $U$. When Fig. 10a and Fig. 10b are examined on the basis of $P_r$, it can be seen that a larger range of weld costs can be accommodated for $P_r = 1.2$. This is more clearly demonstrated in Fig. 10c, which shows the $d_o$ that meet the SunShot Initiative target for various $c_w$. There exist tube diameters for $P_r = 1.5$ that meet the Sunshot target cost, however they are mainly for low $c_w$ and $\dot{m}_f < 2$ kg/s, and the figure is not shown here in the interest of brevity. Due to it accommodating a larger range of $c_w$, having a lower $C_{TES}$, and a higher $Q_{cap}$ (Fig. 8), systems with $P_r = 1.2$ are more favorable than those with $P_r = 1.5$.

Based on the studies performed here, a summary of the most preferred designs that meet the DOE target goal is given in Table 4 for the range of $\dot{m}_f$ considered in this study. Overall, it shows that smaller $d_o$ maximize $U$ and $\psi_D$ while larger $d_o$ minimize $C_{TES}$, which captures the competing effects of total storage cost and $U$. As shown in Table 4a, $U$ is shown to have a preferred design that occurs for the system of $P_r = 1.2$ and $d_o = 0.06$ m (2″ NPS) at $\dot{m}_f = 0.5$ kg/s. As $\dot{m}_f$ increases, $d_o$ must be increased to 0.11 m (4″ NPS) in order to accommodate cost targets and thus a decrease in $U$ and $\psi_D$ is observed. The design point based on maximizing $\psi_D$ (Table 4b) is shown to be variable of $\dot{m}_f$. Low $\dot{m}_f$ correspond to a preferred design point of $P_r = 1.2$ and $d_o = 0.06$ m due to the increased amount of exergy stored within the system allowing for increased exergy recovery. However, the increased $\Delta P$ (Fig. 7b) and decreased residence time at $\dot{m}_f = 3.0$ kg/s leads to increased exergy destruction and decreased $U$, respectively, which causes the preferred design point to shift to a system with $P_r = 1.5$ and $d_o = 0.11$ m. From Table 4c, it is observed that minimum $C_{TES}$ is obtained at a different $d_o$ from that of $U$ and $\psi_D$. Furthermore, for most cases, the cost saturates beyond $d_o = 0.17$ m (6″ NPS) with further increases in $d_o$ from 0.17 m to 0.22 m leading to a maximum cost decrease of 7.94% (Fig. 10a and b). Based on the competing effects of $U$ — which should be maximized — and capital cost — which should be minimized— the preferred design point lies at $P_r = 1.2$ and $d_o = 0.22$ m (8″ NPS), regardless of the $\dot{m}_f$ considered.

In general, these results show that there are preferred design points for a STTB in order to minimize the cost and maximize the

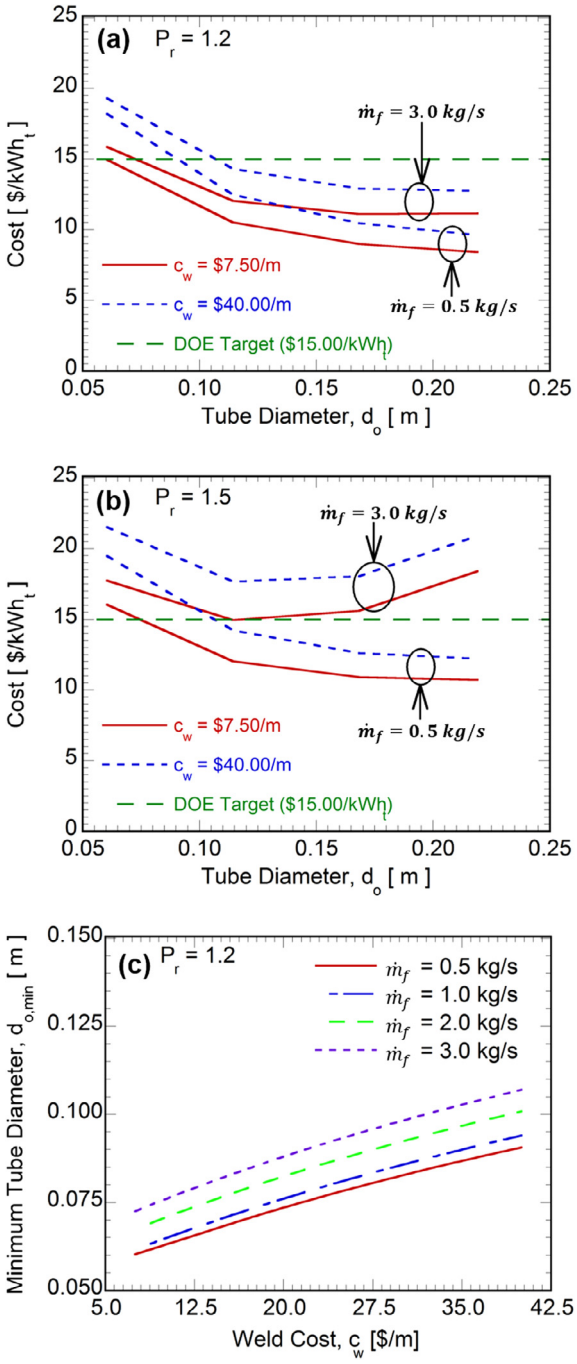


**Fig. 10.** System cost vs tube diameter for systems with (a) $P_r = 1.2$, and (b) $P_r = 1.5$. (c) Minimum tube diameter required to meet SunShot Target cost of $\$15/\text{kWh}_t$ vs welding cost for $P_r = 1.2$.

**Table 4**
Preferred designs that meet the DOE cost goals based on parametric studies. The values of the objective function for the preferred design configurations are presented in bold italics.

| Objective | $\dot{m}_f$ $\left[\frac{kg}{s}\right]$ | $c_w$ $\left[\frac{\$}{m}\right]$ | $U$ [%] | $\psi_d$ [%] | $C_{TES}$ $\left[\frac{\$}{kWh_t}\right]$ | $P_r$ | $d_o$ [m](in.) |
|---|---|---|---|---|---|---|---|
| | 0.5 | 7.50 | ***86.09*** | 95.16 | 14.96 | 1.2 | 0.06 (2″ NPS) |
| | | 40.00 | ***81.00*** | 94.09 | 12.49 | 1.2 | 0.11 (4″ NPS) |
| | 3.0 | 7.50 | ***70.64*** | 77.27 | 12.06 | 1.2 | 0.11 (4″ NPS) |
| | | 40.00 | ***70.64*** | 77.27 | 14.32 | 1.2 | 0.11 (4″ NPS) |
| | 0.5 | 7.50 | 86.09 | ***95.16*** | 14.96 | 1.2 | 0.06 (2″ NPS) |
| | | 40.00 | 81.00 | ***94.09*** | 12.49 | 1.2 | 0.11 (4″ NPS) |
| | 3.0 | 7.50 | 58.59 | ***84.18*** | 14.95 | 1.5 | 0.11 (4″ NPS) |
| | | 40.00 | 70.64 | ***77.27*** | 14.32 | 1.2 | 0.11 (4″ NPS) |
| | 0.5 | 7.50 | 71.63 | 91.44 | ***8.41*** | 1.2 | 0.22 (8″ NPS) |
| | | 40.00 | 71.63 | 91.44 | ***9.62*** | 1.2 | 0.22 (8″ NPS) |
| | 3.0 | 7.50 | 54.00 | 77.43 | ***11.16*** | 1.2 | 0.22 (8″ NPS) |
| | | 40.00 | 54.00 | 77.43 | ***12.76*** | 1.2 | 0.22 (8″ NPS) |

exergetic efficiency – both of which are goals relevant to the DOE SunShot Initiative. While this model already provides useful results for design, future improvements could involve coupling the model to a power cycle to increase the practical understanding that a changing HTF outlet temperature has on plant performance, including a thermal losses model to account for its effect on cost and efficiency, and implementing a more thorough cost model. Overall, there is room for improvement in this model, but it still provides useful information for a designer of a high temperature TES system.

## 6. Conclusions

A two dimensional, unsteady, numerical model was successfully developed and verified for a high temperature sulfur-based shell and tube style thermal energy storage battery system with the storage fluid on the tube-side. The model investigates the performance for important operating and design parameters, such as: variable mass flow rate, tube pitch, tube diameter, and baffle spacing. The performance of the systems was assessed based on the exergetic efficiency, energy utilization, and system cost. Based on the results, the following conclusions can be made:

- The performance metrics are shown to be most sensitive to tube diameter, tube pitch ratio, and mass flow rate.
- The highest energy utilizations, $U$, are seen for tube diameters of 0.06–0.11 m (2″ NPS – 4″ NPS) and tube pitch ratios of 1.2, with a maximum energy utilization of 86.09% for the range of values considered that also meet DOE cost target.
- The maximum exergetic efficiency, $\psi_D$, varies anywhere between 95.16% and 84.18% at the preferred design points which meet DOE cost target. Exergy destruction due to compressor work has a considerable effect at elevated mass flow rates.
- The DOE target goal of \$15/kWh$_t$ is generally met for designs of $d_o > 0.11$ m (4″ NPS) for tube pitch ratio of 1.2 and all considered mass flow rates, with cost based performance saturating beyond $d_o = 0.17$ m (6″ NPS).

Future studies should focus on multi-objective optimization to improve exergetic efficiency and utilization, while reducing system cost, $C_{TES}$.

## Acknowledgment

This effort was supported by the ARPA-E Award DE-AR0000140, Southern California Gas Company Grant Nos. 5660042510, 5660042538, and California Energy Commission Contract No. EPC-14-003.

## References

[1] H.L. Zhang, J. Baeyens, J. Degrève, G. Cacères, Concentrated solar power plants: Review and design methodology, Renew. Sustain. Energy Rev. 22 (2013) 466–481.
[2] S.M. Flueckiger, B.D. Iverson, S.V. Garimella, J.E. Pacheco, System-level simulation of a solar power tower plant with thermocline thermal energy storage, Appl. Energy 113 (2014) 86–96.
[3] K.H. Khan, M.G. Rasul, M.M.K. Khan, Energy conservation in buildings: Cogeneration and cogeneration coupled with thermal energy storage, Appl. Energy 77 (1) (2004) 15–34.
[4] B. Cárdenas, N. León, High temperature latent heat thermal energy storage: Phase change materials, design considerations and performance enhancement techniques, Renew. Sustain. Energy Rev. 27 (2013) 724–737.
[5] P. Wells, K. Nithyanandam, R.E. Wirz, Cost optimal strategies of high temperature thermal energy storage systems in combined heat and power applications, in: Proceeding of the ASME 2016 Power and Energy Conference, 2016.
[6] J. Stekli, L. Irwin, R. Pitchumani, Technical challenges and opportunities for concentrating solar power with thermal energy storage, J. Therm. Sci. Eng. Appl. 5 (2) (2013) 21011.
[7] DOE (US Department of Energy), Sunshot Vision Study, 2012.
[8] L.a. Tse, G.B. Ganapathi, R.E. Wirz, A.S. Lavine, Spatial and temporal modeling of sub- and supercritical thermal energy storage, Sol. Energy 103 (2014) 402–410.
[9] R.E. Wirz, Low-cost thermal energy storage for dispatchable CSP: Critical Project Review Report (No. EPC-14-003), University of California at Los Angeles, Los Angeles, CA, 2016.
[10] H. Rau, T.R.N. Kutty, J.R.F. Guedes de Carvalho, High temperature saturated vapour pressure of sulphur and the estimation of its critical quantities, J. Chem. Thermodyn. 5 (2) (1973) 291–302.
[11] B. Meyer, Elemental sulfur, Chem. Rev. 76 (3) (1976) 367–387.
[12] Personal Communication, California Sulfur Company, August 2016.
[13] 2016, Mineral Commodity Summaries 2016: U.S. Geological Survey, pp. 162–163 [Online]. Available: <http://dx.doi.org/10.3133/70140094>.
[14] Y. Tian, C.Y. Zhao, A review of solar collectors and thermal energy storage in solar thermal applications, Appl. Energy 104 (2013) 538–553.
[15] B. Wong, M. Roeb, D. Thomey, R. Buckingham, L. Brown, C. Sattler, Sulfur based thermochemical energy storage for concentrated solar power, in: Proceeding of the ASME 2013 7th Inernational Conference on Energy Sustainability, 2014, pp. 7–12.
[16] P.D. Clark, N.I. Dowling, Capture of solar energy using elemental sulfur, J. Sulfur Chem. 25 (1) (2004) 7–11.
[17] W.E. Wentworth, E. Chen, Simple thermal decomposition reactions for storage of solar thermal energy, Sol. Energy 18 (3) (1976) 205–214.
[18] R.E. Wirz, A.P.P. Stopin, L.A. Tse, A.S. Lavine, H.P. Kavehpour, R.B. Lakeh, B. Furst, G. Bran-anleu, M.A. Garcia-Garibay, Regents of California, High-density, high-temperature thermal energy storage and retrieval, Patent Application No. US 14/475479, filed Sept 02, 2014.
[19] M. Lacroix, Numerical simulation of a shell-and-tube latent heat thermal energy storage unit, Sol. Energy 50 (4) (1993) 357–367.
[20] Q. He, W.N. Zhang, A Study on Latent Heat Storage Exchangers With the High Temperature Pcm, in: World Renew. Energy Congr. VI, (January 2000), 2000, pp. 1044–1047.
[21] A. Trp, An experimental and numerical investigation of heat transfer during technical grade paraffin melting and solidification in a shell-and-tube latent thermal energy storage unit, Sol. Energy 79 (6) (2005) 648–660.
[22] G.B. Ganapathi, D. Bame, B. Furst, L. Angeles, M. Pauken, R.E. Wirz, A 5 kWht lab-scale demonstration of a novel thermal energy storage concept with supercritical fluids, 2013, pp. 1–9.
[23] L.A. Tse, A.S. Lavine, R.B. Lakeh, R.E. Wirz, Exergetic optimization and performance evaluation of multi-phase thermal energy storage systems, Sol. Energy 122 (2015) 396–408.

[24] N.G. Barton, Simulations of air-blown thermal storage in a rock bed, Appl. Therm. Eng. 55 (1–2) (2013) 43–50.
[25] M. Hänchen, S. Brückner, A. Steinfeld, High-temperature thermal storage using a packed bed of rocks e Heat transfer analysis and experimental validation, Appl. Therm. Eng. 31 (10) (2011) 1798–1806.
[26] N. Mertens, F. Alobaid, L. Frigge, B. Epple, Dynamic simulation of integrated rock-bed thermocline storage for concentrated solar power, Sol. Energy 110 (2014) 830–842.
[27] P. Chandra, D.H. Willits, Pressure drop and heat transfer characteristics of air-rockbed thermal storage systems, Sol. Energy 27 (6) (1981) 547–553.
[28] M. Mehos, C. Turchi, J. Jorgenson, P. Denholm, C. Ho, K. Armijo, On the Path to Sunshot: Advancing Concentrating Solar Power Technology, Performance, and Dispatchability, 2016.
[29] A.L. Avila-Marin, Volumetric receivers in Solar Thermal Power Plants with Central Receiver System technology: A review, Sol. Energy 85 (5) (2011) 891–910.
[30] M. Sheikholeslami, M.M. Rashidi, T. Hayat, D.D. Ganji, Free convection of magnetic nanofluid considering MFD viscosity effect, J. Mol. Liq. 218 (2016) 393–399.
[31] M. Sheikholeslami, D. Domiri Ganji, M. Younus Javed, R. Ellahi, Effect of thermal radiation on magnetohydrodynamics nanofluid flow and heat transfer by means of two phase model, J. Magn. Magn. Mater. 374 (2015) 36–43.
[32] M. Riaz, Analytical solutions for single and two-phase models of packed-bed thermal storage systems, J. Heat Transfer 99 (August) (1977) 489–492.
[33] International Organization for Standardization, 2013, ISO 668:2013 Series 1 Freight Containers - Classifications, Dimensions, and Ratings - Ammendment 1.
[34] T.L. Bergman, A.S. Lavine, F.P. Incropera, D.P. Dewitt, Fundamentals of Heat and Mass Transfer, John Wiley & Sons, 2011.
[35] K. Nithyanandam, A. Barde, R.E. Wirz, Charge and discharge behavior of elemental sulfur in isochoric high temperature thermal energy storage systems, Appl. Energy. (2017) (in review).
[36] W.N. Tuller, Freeport Sulfur Company, The Sulfur Data Book, McGraw-Hill, New York, 1954.
[37] The American Society of Mechanical Engineers, Welded and Seamless Wrought Steel Pipe, The American Society of Mechanical Engineers, New York, 2015.
[38] S.V. Patankar, Numerical Heat Transfer and Fluid Flow, 1980.
[39] D.Q. Kern, Process Heat Transfer, McGraw-Hill, 1990.
[40] K. Bell, Final Report of the Cooperative Research Program on Shell-and-tube Heat Exchangers, 1963.
[41] M.J.N. Wills, D. Johnson, A New and Accurate Hand Calculation method for Shell-Side Pressure Drop and Flow Distribution, 22nd Nat. Heat Transfer Conf., ASME, New York, 1984.
[42] K. Bell, D. Chisholm, A. Cooper, Heat Exchanger Design Handbook, Hemisphere Publishing Corporation, 1983.
[43] J. Taborek, Shell-and-tube heat exchangers, Heat Exchanger Design Handbook, vol. 3. Hemisphere Publishing Corporation, New York, 1988.
[44] M.J. Moran, H.N. Shapiro, D.D. Boettner, M.B. Bailey, Fundamentals of Engineering Thermodynamics, John Wiley & Sons, 2011.
[45] M.A. Shinn, Design and Performance Analysis for a Sulfur-Based Thermal Energy Storage System using Intermodal Containment, 2016.
[46] R.E. Wirz, Thermal Energy Storage with Supercritical Fluids (Grant No. DOE-UCLA-AR000140), 2017.
[47] J.T. Van Lew, P. Li, J. Stephens, Analysis of Heat Storage and Delivery of a Thermocline Tank, 133, May 2011, pp. 1–10.
[48] M.A. Rosen, Appropriate Thermodynamic Performance Measures for Closed Systems for Thermal Energy Storage, 114 May 1992.
[49] Z. Yang, S.V. Garimella, Thermal analysis of solar thermal energy storage in a molten-salt thermocline, Sol. Energy 84 (6) (2010) 974–985.
[50] S. Kakac, H. Liu, Heat Exchangers: Selection, Rating, and Thermal Design, CRC Press, 2002.
[51] Tubular Exchanger Manufacturers Association Inc, Standards of the Tubular Exchanger Manufacturers Asscociation, Tarrytown, NY, 1999.
[52] Certilas Nederland BV, Certilas Welding Software, 2016.
[53] C. Turchi, P. Kurup, S. Akar, F. Flores, C. Turchi, P. Kurup, S. Akar, Domestic Material Content in Molten-Salt Concentrating Solar Power Plants Domestic Material Content in Molten-Salt Concentrating Solar Power Plants, August 2015.
[54] Personal Communication, BSL Container, November 2016.